Well-defined nanostructuring with programmable anodic aluminium oxide template

Rui Xu
Ilmenau University of Technology
Zhiqiang Zeng
Ilmenau University of Technology
Yong Lei (yong.lei@tu-ilmenau.de)
Ilmenau University of Technology https://orcid.org/0000-0001-5048-7433

Article

Keywords: nanostructuring, technology

Posted Date: April 7th, 2021

DOI: https://doi.org/10.21203/rs.3.rs-351547/v1

Well-defined nanostructuring with programmable anodic aluminium oxide template

Authors: Rui Xu, Zhiqiang Zeng, Yong Lei*

Affiliations: Fachgebiet Angewandte Nanophysik, Institut für Physik & IMN MacroNano, Technische Universität Ilmenau, Ilmenau 98693, Germany.

*e-mail: yong.lei@tu-ilmenau.de

Abstract: Well-defined nanostructuring over size, shape, spatial configuration, and multi-combination is a feasible concept to reach unique properties of nanostructure arrays, while satisfying such broad and stringent requirements with conventional techniques is challenging. Here, we report programmable anodic aluminium oxide templates to address this challenge by achieving well-defined pore features within templates in terms of in-plane and out-of-plane shape, size, spatial configuration, and pore combination. The structural programmability of template pores arises from broad-range anodization voltage adjusting together with uneven aluminium anodization rate designing, and further relies on a systematic blueprint guiding pore diversification. Starting from the programmable templates, we realize a series of nanostructures that inherit equal structural controllability relative to their template counterparts. Proof-of-concept applications based on such nanostructures demonstrate boosted performance. In light of the broad selectivity and high controllability, programmable templates will provide an all-in-one platform for well-defined nanostructuring.

Due to the compelling requirement of device miniaturization, synthesis of nanoscopic structures and their macroscopic integration into a large-scale array are fundamental to modern and future devices in the fields of optics[1], electronics[2], telecommunication[3], biology[4], and energy conversion/storage[5,6], etc. It is known that nanostructures are subject to physical and chemical property variation as a function of their geometry and composition[7]; and arrayed assemblies of these nanostructures exhibit collective behaviors of their responses in terms of coupling in the same set and synergy between different sets[8,9]. Therefore, to tailor the overall properties of a nanostructure array (hence to foster devices based on this nano-array), it is highly desirable to achieve well-defined nanostructuring that is capable of precise controlling over the structural parameters of a nanostructure array. As such, six capabilities could be indispensable for an efficient well-defined nanostructuring technique: i) ability to assemble nanostructures into a large-scale array with cost-effective processes; ii) reliable size controllability as well as iii) in-plane and iv) out-of-plane shape programmability of the nanostructures; v) alterability of the spatial configuration (or arrangement) of nano-arrays; vi) compatibility of different sets of arrayed nanostructures with tunable shape and configuration of each set. Various nanostructuring techniques have been developed, such as photo/electron-beam lithography, self-assembly, nanoimprinting, and template-based techniques[10], while almost none of these techniques fulfills all the above six capabilities of well-defined nanostructuring.

The template-based technique, especially of using anodic aluminium oxide (AAO) nanoporous template, has attracted high attention for nanostructuring[11], because it fully satisfies the aforementioned first and second capabilities: i) enabling integration of millions of nanostructures into large-scale arrays in a cost-effective way[12]; ii) AAO pores along with the replicated nanostructure arrays are well controlled in size[13,14]. However, other four capabilities (iii-vi) are missing for AAO templates. To our best knowledge, only a handful of shapes are available for

pores (e.g., circular, triangular, and square)[15-17], and the spatial configurations of pores are quite limited (e.g., the trigonal, tetragonal, and hexagonal arrangements with identical interpore spacing) because of the linear relationship between pore spacing and anodization voltage (AV)[18]. Binary-pore AAO templates enable two sets of nanostructures into one matrix[19], however the shape- and arrangement-selectivity of pores are still limited, and consequently few combinations are achievable. Therefore, to realize well-defined nanostructuring based on template-based techniques, breakthroughs must be made from the functional limitation of the existing AAO templates, especially to endow the templates with both broad selectivity (in pore shape, pore spatial configuration, and pore combination) and high controllability (in each parameter).

Here, we realize programmable AAO templates with state-of-the-art controllability over in-plane and out-of-plane pore shape, spatial configuration of pore arrangement, and pore combination. Compared to a conventional template with a single pore shape in a specific spatial configuration, the in-plane pore shape of the programmable template can be continuously altered from polygons (e.g., triangle and square) with internally-bent walls to polygons with non-bent walls and then to polygons with externally-bent walls, by applying a range of AVs (rather than a specific AV, following the above linear spacing-AV relationship) upon uneven-profiled aluminium nanodents. These pore shapes can be integrated into one pore along the axial direction under sequential anodic anodization at different AVs, forming multi-segment pores with different out-of-plane shapes. The programmable templates are also capable of mixing diverse arrangements and spacings of pores into one matrix by virtue of broad-range AV adjustability, successfully pushing the selection in spatial configuration beyond the aforementioned limitations. Additionally, different sets of in-plane and out-of-plane shape-programmable pores can be interlaced by a subsequent wet-chemical etching procedure, forming a series of pore combinations. Importantly, the structural controllability of the programmable templates is totally transferable into their

nanostructure counterparts, achieving a large quantity of (size-, shape-, spatial configuration-, and combination-) well-defined nanostructures (nanoparticles, nanotubes, nanowires, and nanomeshes) which enable device performance optimization that is demonstrated in three proof-of-concept applications.

Programming in-plane pore shape by adjusting anodization voltage

The in-plane pore shape programmability of AAO templates originates with a scenario of designing uneven aluminium anodization rates at different AVs. Electric field (EF) maps in an aluminium foil decorated with a tetragonal array of four-leaf clover-like nanodents (namely uneven profile, see layout of COMSOL simulation in Supplementary Fig. 1) were simulated to elucidate how one can control pore shape. Obviously, high EF sites are located at the bottom of nanodents (Fig. 1a) and eight spots on the walls (Fig. 1b). Considering a widely-accepted field-assisted dissolution theory in which aluminium anodization is preferably conducted at high EF sites[20], here anodization will proceed not only at the bottoms of nanodents but also on the walls, resulting in axial anodization imposing on pore elongation and radial anodization dictating shape evolution. As shown in Fig. 1b, apart from eight stronger-EF spots, each nanodent has weaker EF at four humps, leading to uneven EF distribution and consequently uneven radial anodization rates. With the AV increasing, the absolute EF difference between eight spots and four humps gets larger (Supplementary Fig. 2). Given that more acid anions are driven into the oxide layer by higher EFs and that the quantity of incorporated acid anions is positively related to volume expansion[20,21], it is predicted that larger volume expansion difference at higher AVs should lead to smoother and more externally-bent walls, vice versa sharper and more internally-bent ones at lower AVs (please refer to Supplementary Fig. 3). This prediction of AV-dependent pore shape programmability is fully confirmed by the following experimental results.

Fabrication process of a proof-of-principle template is schematically depicted in Fig. 1c, which generally includes two sequential procedures of imprinting and anodization. A purposely-designed Ni imprint stamp decorated with four-leaf clover-like nanopillars on its surface (Supplementary Fig. 4) was used for predetermining sites on the aluminium surface to guide pore evolution (Supplementary Fig. 5). Anodization was then performed with four different AVs: at 120 V, the anodized pores were cross-shaped with internally-bent walls (Fig. 1d and Supplementary Fig. 6a); with 140 V, the internally-bent amplitude was suppressed to form star-like pores (Fig. 1e); at 160 V, the pore wall became straight without bending, achieving square-shaped pores (Fig. 1f); when the AV was 200 V, the pores presented a circular shape, analogous to a square shape with its walls being externally-bent (Fig. 1g and Supplementary Fig. 6b). To test the applicability of the pore shape programmability to other arrangements, we also made a hexagonal array of three-leaf clover-like nanodents (Supplementary Figs. 7 and 8). It was found that also guided by uneven EFs (Supplementary Fig. 9d), the anodized pores possessed a similar shape-programming trend to that of the tetragonal array. For example, the triangular pore shape without bending obtained at 140 V (Fig. 1j and Supplementary Fig. 10a) was changed to a wall-internally-bent triangular shape at a lower AV of 120 V (Fig. 1i) and further evolved to a more wall-internally-bent triangular shape when the AV was decreased to 100 V (Fig. 1h and Supplementary Fig. 10b); when the AV was increased to 155 V, it demonstrated a wall-externally-bent shape (Fig. 1k). To explore appropriate AV values, we performed anodization in a broader AV range thereafter. It is found that concerning a specific arrangement, the adjustable AV for programming pore shape is limited in an AV range (denoted as appropriate AV range), out of which the arrangement predetermined by nanodents is broken (see details in Supplementary Figs. 11,12). This in-plane shape-programmable technique is applicable for large-scale fabrication, as evidenced by a template with a 2.5-cm-diameter area (Supplementary Fig.

13). The green color, spreading over the whole anodized area (left image of Fig. 1l), implies high structural uniformity of the pore array which is verified by a large-area 40-μm-width scanning electron microscope (SEM) image (right part of Fig. 1l) and a nearly monodisperse pore size distribution (Supplementary Fig. 14). Here, for each pore arrangement we just selected four AVs and obtained four pore shapes. Of course, the rest of values within the appropriate AV range are selectable for tuning pore shape and consequently more pore shapes should be achievable.

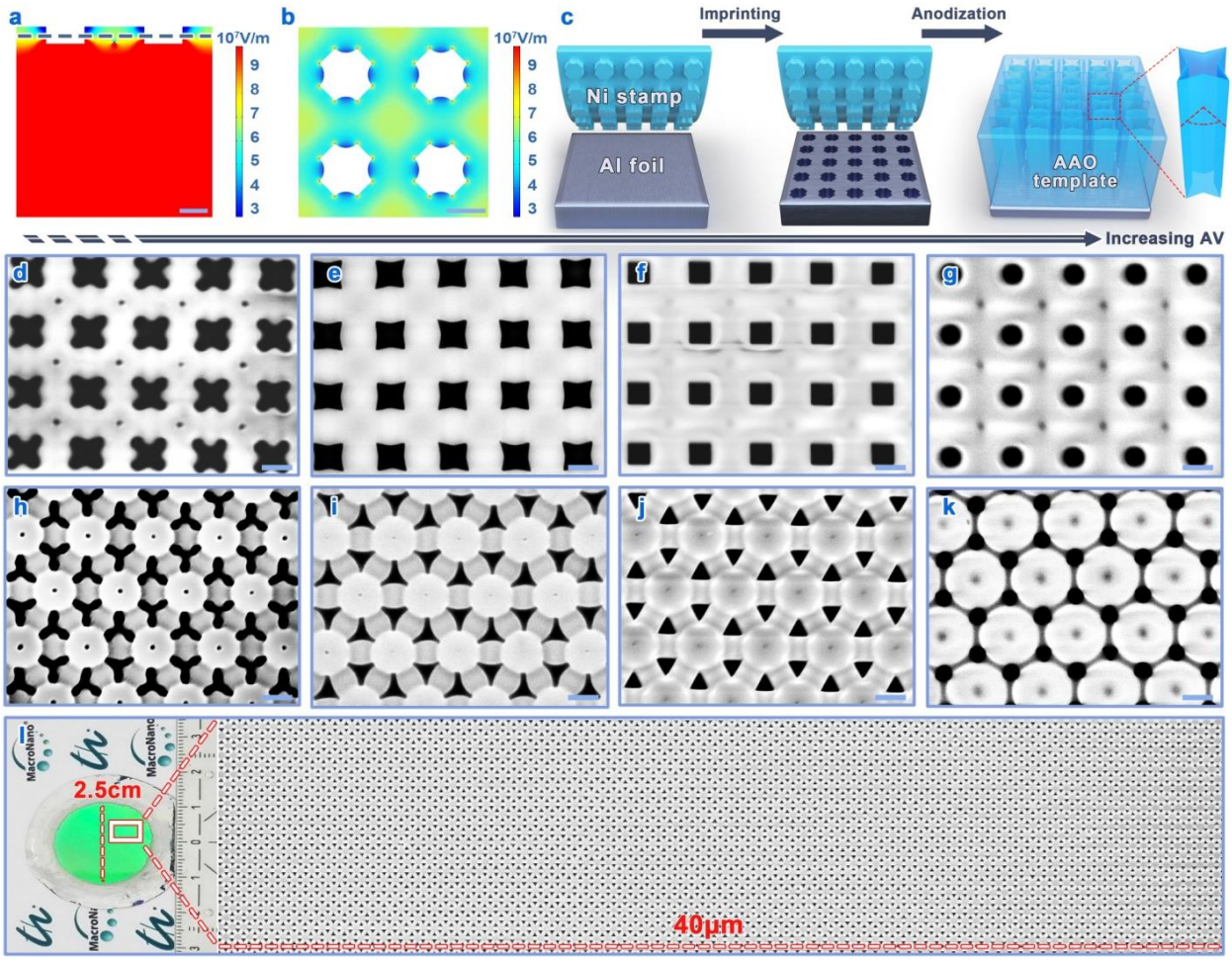

Fig. 1 | Templates with in-plane shape-programmable pores. a,**b**, COMSOL-simulated electric fields at (**a**) vertical cross section and (**b**) near-surface lateral cross section of an aluminium foil patterned with four-leaf clover-like nanodents of 400-nm spacing and tetragonal arrangement under an anodization voltage (AV) of 120 V, the dashed line in (**a**) at the half-depth

of nanodents marks the near-surface lateral cross section in (**b**). **c**, Schematic illustration for the fabrication process of AAO template (from left to right): fabricating Ni imprint stamp and electro-polishing aluminium foil; transferring the structural feature of Ni stamp by imprinting to equip aluminium surface with an array of four-leaf clover-like nanodents; anodizing the imprinted area at different AVs. **d**-**k**, SEM images of templates with shape-programmable pores in (**d**-**g**) tetragonal and (**h**-**k**) hexagonal arrangements. Two arrangements are 400 and $400/\sqrt{3}$ nm in spacing, respectively (see Supplementary Figs. 4,7). From left to right, the exploited AVs were incrementally increased, with (**d**) 120 V, (**e**) 140 V, (**f**) 160 V, (**g**) 200 V; and (**h**) 100 V, (**i**) 120 V, (**j**) 140 V, (**k**) 155 V, respectively. **l**, Optical photograph of 2.5-cm-diameter AAO template (left) and large-area SEM image (right). Scale bars: 200 nm.

Programming out-of-plane pore shape with sequential anodization voltages

To further advance the pore shape programmability, we also made efforts towards tuning the out-of-plane shape. Using the tetragonal template as an example, Fig. 2 demonstrates how to program pore shape in the axial direction by multi-step anodization with different AVs. For the template I in Fig. 2 that was anodized at 120 V, the cross-shaped pores remain identical from top to bottom. When two AVs of 120 and 200 V were sequentially applied to prepare the template II, its pores contain two segments: the first segment at the top has a cross shape while the second at the bottom has a circular shape. Although the first segment was exposed to higher AV during the second-step anodization, the cross-pore shape remained unchanged, indicating that the shape in each segment is independent. This independence imparts more diverse axial pore shape programmability, as reflected by the template III that has three segments of each pore: star, square, and circular shapes corresponding to the AVs of 140, 160, and 200 V, respectively. In addition to the adjusting trend from low to high AVs, we can also perform multi-step anodization

in the opposite direction, for example, to further carry out multi-step anodization on the template IV (from 200 to 160 V) and the template V (from 200 to 160 and then 140 V). Accordingly, template IV with four segments (star+square+circular+square) and template V with five segments (star+square+circular+square+star) were fabricated. It is foreseeable that templates with more selections of out-of-plane pore shapes, as well as the resultant one-dimensional shape-different multi-segment nanostructures (see examples in Supplementary Fig. 15, Fig. 6e-h), are achievable by selecting different series of AVs in the appropriate AV range.

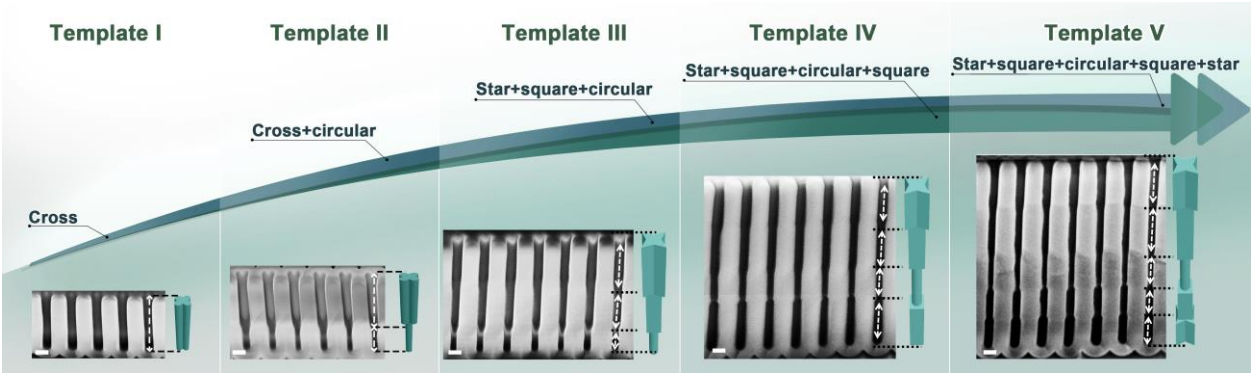

Fig. 2 | Templates with out-of-plane shape-programmable pores. Cross-sectional SEM images and the corresponding pore schematics (on the right of each SEM figure) of templates I – V with different out-of-plane pore shapes. From left to right: the sequentially exploited AVs (and the pore shapes) are Template I: 120 V (cross); Template II: 120→200 V (cross+circular); Template III: 140→160→200 V (star+square+circular); Template IV: 140→160→200→160 V (star+square+circular+square); Template V: 140→160→200→160→140 V (star+square+circular+square+star), respectively. Scale bars: 200 nm.

Designing pore shape within mixture arrangement

Given that pore shapes are highly dependent on the spatial configuration of neighboring pores (Supplementary Fig. 16 for details)[16] and also considering that only three equilateral polygons tile

a plane without gap (please refer to Supplementary Fig. 17), it is imperative to configure mixture arrangements for achieving more spatial configurations and thus more shapes of pores. Considering the preceding observation that AVs for a specific arrangement are limited within an appropriate AV range (Supplementary Fig. 12), we hypothesized that AVs of a mixture arrangement should lie in an intersection of several appropriate AV ranges to remain every constituent arrangement. To test this hypothesis, we mixed the above tetragonal arrangement with a larger-spacing tetragonal arrangement, and their corresponding AV intersection should be from 160 V to about 226 V (Supplementary Fig. 18 for details). When an AV of 190 V within the intersection was exploited, both arrangements were maintained (Fig. 3a); in contrast, the long-spacing arrangement at an AV of 158 V below the intersection was absent with the occurrence of new pores at the central sites (Supplementary Fig. 19). As mixing with the octagonal arrangement, two arrangements have no overlapping AVs (see Supplementary Fig. 20). Accordingly, a big circular pore (red) was born automatically at the center of the octagonal arrangement under 190-V AV (Fig. 3b). The mixture arrangement is scalable, as evidenced by Fig. 3g where two spacing-different arrangements alternatively tile the whole plane. All experimental results are matched with the prediction, thus validating this hypothesis.

Within mixture arrangements, pores with additional shapes were realizable and further tuned by adjusting AV. For example, besides circular pores (green) in the basic arrangement, elliptical pores (cyan) were observed in the accessory arrangements (Fig. 3a,b). The elliptical shape with higher structural asymmetry may stem from the competition between neighboring arrangements exerted by different anodization rates[22], as evidenced by nonuniform EF distribution therein (Supplementary Fig. 21). Likewise (see Supplementary Fig. 22), three-pointed star-shaped pores (blue, Fig. 3c) were realized in the centered tetragonal arrangement at 140-V AV. The accessory arrangements can be inserted in the form of line (Fig. 3d), area (Fig. 3e), and even complex

pattern (Fig. 3f) as well, achieving other shapes such as isosceles triangular (yellow), rectangular (orange), and semi-circular (purple). Similarly, these new shapes are changeable by adjusting AV. For example, the pores owning the same spatial configuration (Supplementary Fig. 23) were varied from the non-bent (yellow, Fig. 3d) to the wall-externally-bent (yellow, Fig. 3f) triangular shape as increasing AV from 190 to 210 V. More pore shapes will be obtainable by configuring other mixture arrangements, no matter whether or not their constituents are of the same spacing as long as they possess intersectional AVs.

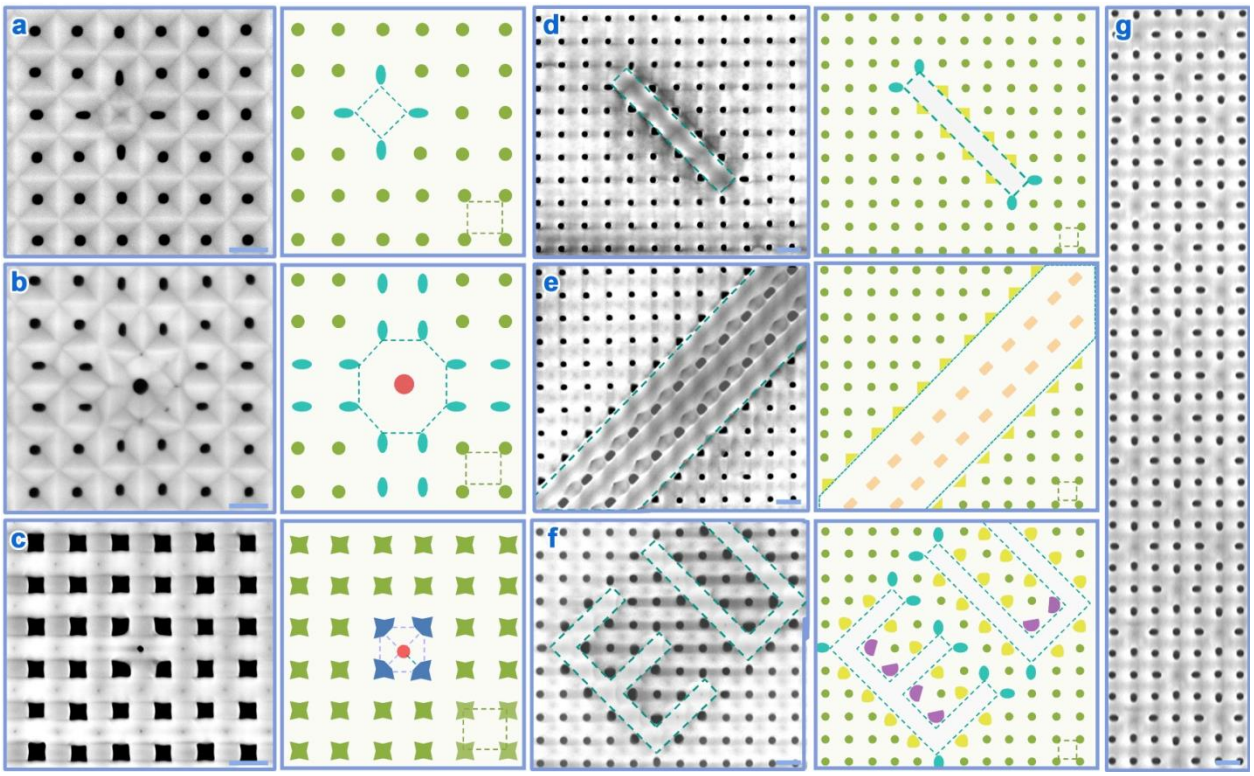

Fig. 3 | Templates with mixture arrangements. a-f, SEM images (left) and schematics (right) of basic tetragonal templates mixed with accessory point units of (**a**) larger-spacing tetragonal arrangement, (**b**) octagonal arrangement, and (**c**) centered tetragonal arrangement, as well as (**d**) line, (**e**) area, and (**f**) pattern 'EU' of larger-spacing tetragonal arrangements. The pores in the basic arrangement are exhibited by green color, and those pores in accessory arrangements are by

cyan, red, blue, yellow, orange, and purple colors. **g**, Large-area SEM image of a mixture of two spacing-different tetragonal arrangements. Scale bars: 400 nm.

Combining different sets of pores with independent shape programmability

In addition to well-defined structural controlling for one set of pores, we also assembled different sets of pores into one template with independently programmable pore shape for each set. Through a wet-chemical etching, a 2nd set of pores was obtained and reshaped at the junction sites of the existing 1st-set pores of the above templates (Supplementary Fig. 24). Taking the tetragonal pore-arrangement template as an example, the 2nd-set pores obtained four different shapes: when etching in NaOH solutions, the pores were isotropically enlarged from a circular shape (Fig. 4b$_1$) to a circular shape truncated with 4 voids (Fig. 4b$_2$); while using H_3PO_4 solutions, the pores were selectively etched from a 4-edged (Fig. 4b$_3$) to an 8-edged cross shape (Fig. 4b$_4$). Similar pore-programming behavior applies to the hexagonal array, as evidenced by a circular shape (Fig. 4d$_1$) and a circular shape with 6 voids (Fig. 4d$_2$) etched in NaOH solutions, as well as a 6-edged cross shape (Fig. 4d$_3$) and a 12-edged cross shape (Fig. 4d$_4$) etched in H_3PO_4 solutions. By assembling the 1st-set pores (green) in Fig. 4a,c and the related 2nd-set pores (cyan) in Fig. 4b,d into one matrix, we have achieved 2×3×4 pore shape combinations, as summarized in Fig. 4a$_i$b$_j$ (i = 1 to 3, j = 1 to 4) and Fig. 4c$_m$d$_n$ (m = 1 to 3, n = 1 to 4). These pore combinations exhibit large-area uniformity as well (Supplementary Figs. 25,26). Besides the shape programmability in the axial direction for the 1st-set pores (outlined by green dashed line), the out-of-plane shape of the 2nd-set pores (outlined by cyan dashed line) can also be programmed (Fig. 4e), probably because the walls formed at different AVs have inhomogeneous composition and thus etching rates (Supplementary Fig. 27)[23].

Taking this concept a step further, we realized different-set multi-shape pore combinations within mixture arrangements (Fig. 4f,g). For example, starting from the mixture array with point of accessory arrangement (Fig. 3a), wet-chemical etching gave rise to two types of pores with the same 4-edged cross shape but dissimilar orientations (cyan and pink), producing a two-set 4-shape template. Similarly, by etching the mixture array with area of accessory arrangements (Fig. 3b), pores of differently-oriented 4-edged cross (cyan and purple) and 3-edged cross (red) shapes were obtained, leading to two-set 6-shape templates together with the 1st-set pores of circular (green), rectangular (blue), and isosceles-triangular (orange) shapes (Fig. 4g).

In general, the total number of structural selection for templates with one-set pores and pore combinations could be estimated by the following equation:

$$f\left(x,y,z\right)=\sum_{i=1}^{x}\left(y_i+z_i+y_i\times z_i\right) \tag{1}$$

where i: the serial number of a specific spatial configuration of pores; x: the number of spatial configurations for the 1st-set pores which in principle need to satisfy the criterion that all constituent arrangements have an intersectional AV range; y: the number of the in-plane and out-of-plane shapes of the 1st-set pores determined by AV adjustable range and AV adjustable sequence; z: the number of the 2nd-set pore shapes controlled by wet-chemical etching.

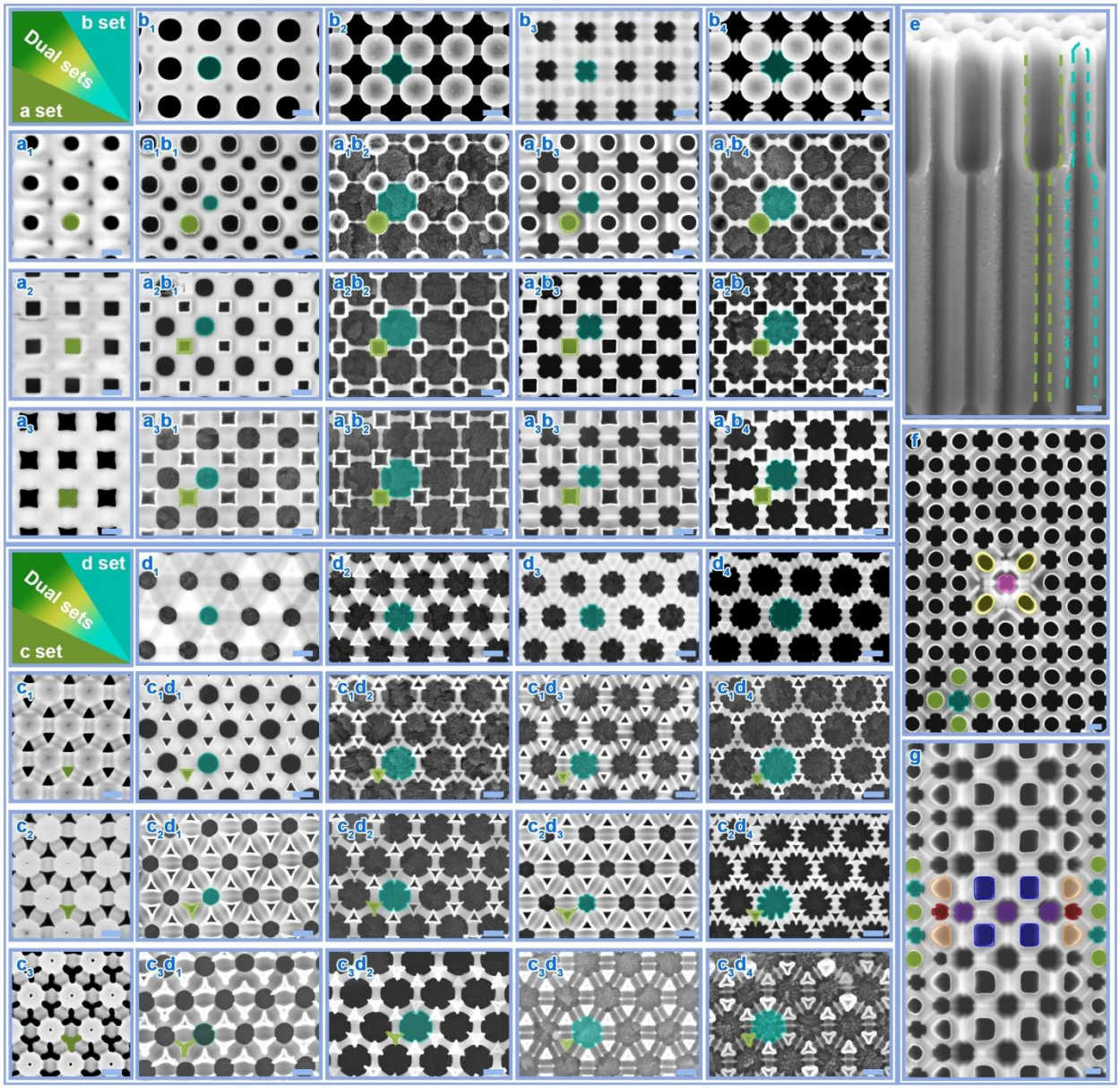

Fig. 4 | Templates with shape-programmable pore combinations. $\mathbf{a}_i\mathbf{b}_j$, Pore combinations, with the 1st-set pores (of tetragonal arrangement, green color) in ($\mathbf{a}_i$) (similar to the pores in Fig. 1e-g) and the 2nd-set pores (of tetragonal arrangement, cyan colors) in ($\mathbf{b}_j$). The 1st-set and 2nd-set pores were formed before and after the wet-chemical etching procedure, respectively (please refer to Supplementary Fig. 24). $\mathbf{c}_m\mathbf{d}_n$, Pore combinations, with the 1st-set pores (of hexagonal arrangement, green color) in ($\mathbf{c}_m$) (similar to the pores in Fig. 1h-j) and the 2nd-set pores (of trigonal arrangements, cyan colors) in ($\mathbf{d}_n$). **e**, Pore combinations with two sets of out-of-plane

dual-shape pores outlined by green (1st-set pore) and cyan (2nd-set pore) dashed lines. The anodization for growing the 1st-set pores was performed under sequential AVs of 140→200 V. **f**,**g**, Multi-shape pore combinations within mixture arrangements, stemming from the tetragonal templates mixed with point (Fig. 3a) and area (Fig. 3e) units of accessory arrangements. Colors of green/yellow/orange/blue and colors of cyan/pink/purple/red indicate pores formed before and after the wet-chemical etching procedure, respectively. Scale bars: 200 nm.

Well-defined nanostructure arrays prepared by using programmable templates

Template with programmability of in-plane and out-of-plane pore shape, mixture arrangement and pore combination should be the key for realizing well-defined nanostructures. Various material-synthesis techniques for conventional AAO templates are totally applicable for programmable templates[24-27], by which different well-defined nanostructures can be fabricated such as nanoparticles, nanotubes, nanowires, nanomeshes, and their combinations. As an example, 3 tetragonal templates with 1st-set circular-shaped pores (Figs. 1g and 4a_1), 2nd-set 4-edged cross-shaped pores (Fig. 4b_3), and the corresponding two-set pore combination (Fig. a_1b_3) were used to achieve 11 nanostructure arrays (Fig. 5 and Supplementary Figs. 28-34) including: nanoparticles, nanowires, and nanotubes (Fig. 5a_1-a_3) that all feature circular shape, inherited from the 1st-set pores (Fig. 5a_0); nanoparticles, nanowires, and nanotubes (Fig. 5b_1-b_3) that replicate the 4-edged cross-shape of the 2nd-set pores (Fig. 5b_0); nanoparticles/nanoparticles, nanowires/nanowires, nanowires/nanotubes, nanotubes/nanotubes, and dual-pore nanomesh (Fig. 5c_1-c_5) that combine the shapes of both pores (Fig. 5c_0). Many other well-defined nanostructures are also obtainable by using programmable templates, as well as in conjunction with other synthetic techniques such as on-wire lithography and coaxial lithography[28-30]. In principle, the

number of well-defined nanostructures stemming from programmable templates can be described by:

$$f\left(x,y,z,a,b,c\right)=\sum_{i=1}^{x}\left(a_i\times y_i+b_i\times z_i+c_i\times\left(y_i\times z_i\right)\right) \quad (2)$$

where *a, b, c*: the numbers of the nanostructures replicated from the 1st-set pores, the 2nd-set pores, and the two-set combinations respectively (e.g., *a*, *b*, *c* in Fig. 5 are 3, 3, and 5); *i*, *x*, *y*, and *z* have the same definitions as those in the Equation 1.

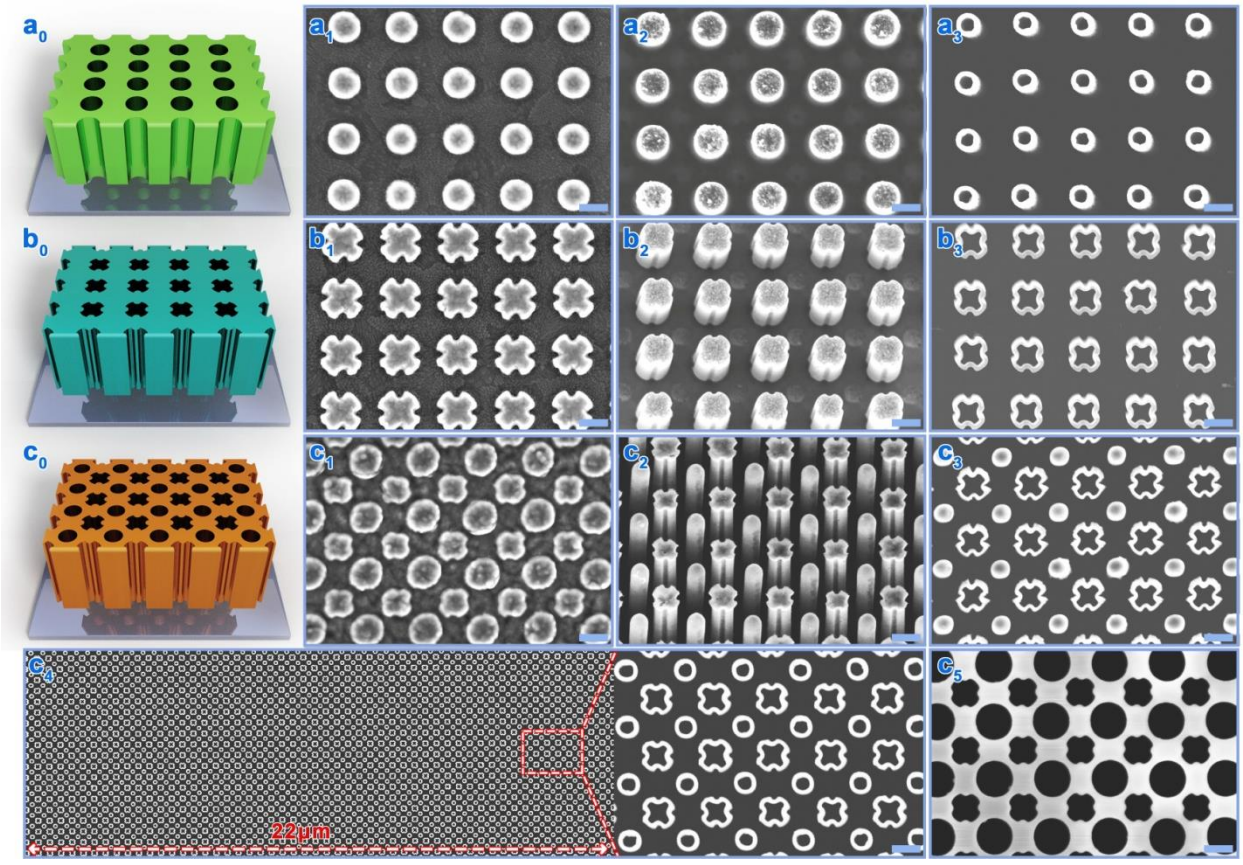

Fig. 5 | Nanostructure arrays replicated from programmable templates. (**a_0**) Schematic of the template with the 1st-set circular pores and SEM images of the resultant nanostructure arrays: (**a_1**) Au nanoparticles, (**a_2**) Ni nanowires, and (**a_3**) TiO_2 nanotubes. (**b_0**) Schematic of the template with the 2nd-set 4-edged cross-shaped pores and SEM images of the resultant nanostructure

arrays: (**b**$_1$) Au nanoparticles, (**b**$_2$) Au nanowires, and (**b**$_3$) SnO_2 nanotubes. (**c**$_0$) Schematic of the template with the two-set pores and SEM images of the resultant nanostructure combinations: (**c**$_1$) Au-nanoparticles/Au-nanoparticles, (**c**$_2$) Pt-nanowires/Au-nanowires, (**c**$_3$) Pt-nanowires/SnO_2-nanotubes, (c$_4$) TiO_2-nanotubes/SnO_2-nanotubes, (**c**$_5$) Ni dual-pore nanomesh. Scale bars: 200 nm.

Application of well-defined nanostructures replicated from programmable templates

Well-defined nanostructures with high freedom of structural programmability could result in some unique and promising properties which are in favor of device utilization. Here we show three envisaged applications of nanostructures arrays prepared by the programmable templates.

The first application is to optimize surface-enhanced Raman spectroscopy (SERS) using five hexagonal arrays of in-plane shape-different Ag nanoparticles (Fig. 6a and Supplementary Fig. 35). Figure 6d shows Raman spectra of Rhodamine 6G molecules chemisorbed on Ag nanoparticles. Compared to the nanoparticles with externally-bent shape (S1), the nanoparticles with non-bent triangular shape (S2) demonstrated a noticeable enhancement in Raman peak intensity. The highest intensity was achieved for the nanoparticles with internally-bent shape (S3), for example, the peak intensity at 1650 cm^{-1} increased by approximately 6.6 times relative to that of S1. With further increasing of the internally-bent amplitude (S4 and S5), the SERS intensities were diminished. Finite-difference time-domain (FDTD) simulations demonstrate that hot spots with strong EFs, stemming from the plasmonic resonance effect[31], are situated around the vertexes of triangles (Fig. 6b). Particularly, the trend of the maximum EF values at the hot spots for five samples is consistent with that for the SERS intensity variation (Fig. 6c), implying that EFs enhanced by the programmable nanoparticle shapes should be the determinative factor of SERS performance.

Then, we investigated the out-of-plane shape-programmable Au nanowires as broadband light absorbers. We fabricated five samples (S6 to S10) which included 1 to 5 shapes respectively, as schematically represented by the insets of Fig. 6h. A nanowire of S10 is shown in Fig. 6e, comprising five different shapes in the axial direction. An overall observation from the optical photographs is the gradual color variation from red to black (Fig. 6f), proving that the reflection of light impinging upon Au nanowires was suppressed with increasing shapes of nanowires. Light absorption efficiencies in the visible range increase monotonically from S6 to S10 (Fig. 6h), which agrees well with the visual observation. Figure 6g shows that strong EFs induced by the plasmonic resonance at short wavelengths (e.g., 500 and 540 nm) are situated at the top parts of the nanowires, that is, in the vicinity of the circular, superelliptic, and square segments. Regarding the long-wavelength illumination, the territory with EF enhancement moves down along the axis (e.g., at 580 and 750 nm) and finally centralizes around the star-like and cross-shaped segments (e.g., at 900 nm). Thus, multiple plasmonic modes are excited within different segments at various wavelengths and work complementarily to achieve strong light absorption in a broad regime.

Finally, we exploited the independent controlling over two-set TiO_2-nanotubes/Au-nanowires combination to promote photoelectrocatalysis. Circular (S11), square (S12), and star (S13) shapes were fabricated for optimizing TiO_2 nanotubes (Fig. 6i), which obtained different H_2 generation rates (Fig. 6k). The discrepancy is primarily ascribed to the variation in light trapping capability (Fig. 6j,l). Then, two shapes of four-void circular (S14) and eight-edged cross (S15) were fabricated for optimizing Au nanowires (Fig. 6i and Supplementary Fig. 36). Reliable H_2 growth was detected for the combinations under visible light, especially for S15 with 4.2 ± 0.7 μmol h^{-1} cm^{-2} (Fig. 6k). This long-wavelength response arises from plasmonic hot-electron injection from Au nanowires to TiO_2 nanotubes[32], as identified by three absorption peaks at 600, 680, and 740

nm (Fig. 6l). Figure 6j shows that EF enhancement tends to concentrate at the voids of Au nanowires, which accounts for the superior performance of S15 over that of S14 due to the occupation of twofold voids in Au nanowires. With optimization for both materials, S15 obtained a H_2 growth rate of 17.5±1.5 μmol h^{-1} cm^{-2} under AM 1.5G illumination, which resulted in about 3.5 times enhancement relative to S11.

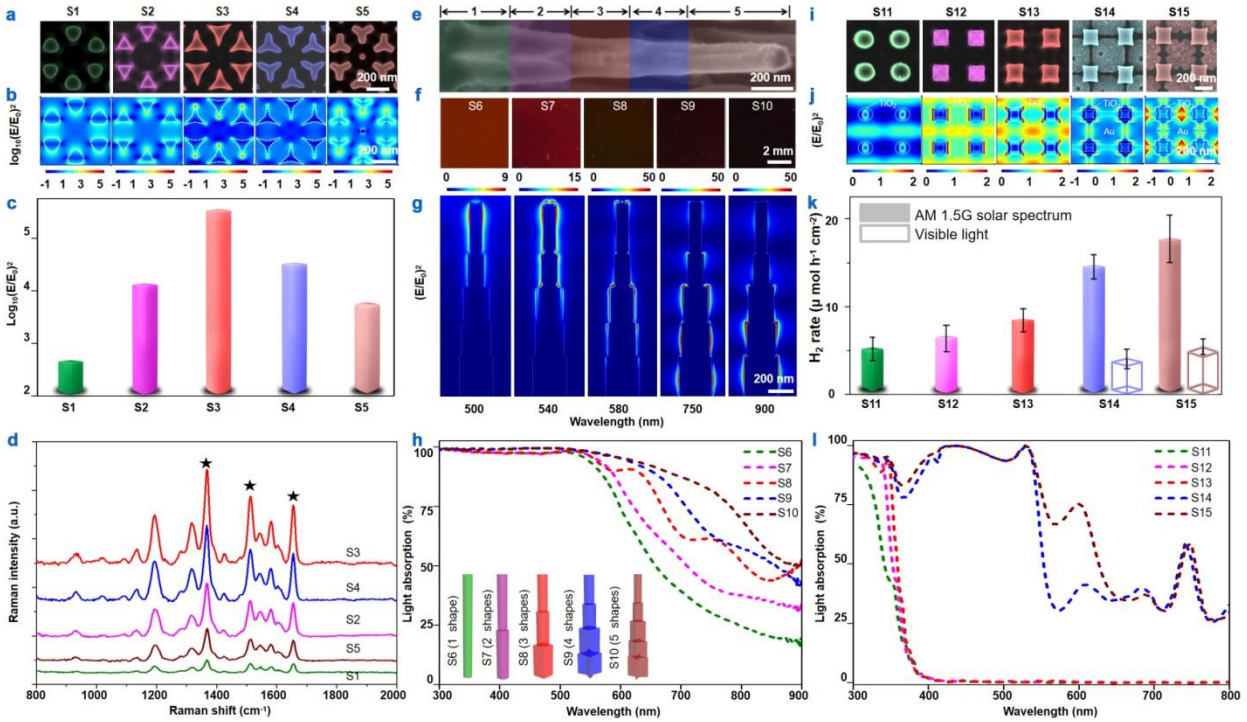

Fig. 6 | Applications of well-defined nanostructures. a-d, SERS characterization with five hexagonal arrays of in-plane shape-different Ag nanoparticles (S1 to S5). (**a**) SEM images of unit cells and (**b**) FDTD-simulated EF intensities (logarithmic scale, 532-nm wavelength illumination). (**c**) The maximal magnitudes of EF intensities in (**b**). (**d**) SERS spectra with three main peaks at 1363, 1508, and 1650 cm^{-1} for Rhodamine 6G molecules chemisorbed on Ag nanoparticles. **e-h**, Light absorbers using five tetragonal arrays of out-of-plane shape-different Au nanowires (S6 to S10). (**e**) SEM image of 5-shape-combined Au nanowire of S10 combining 5 shapes in the axial direction (from left to right): cross, star, square, superelliptic, and circular. (**f**)

Optical photographs of S6 to S10, involving Au nanowires of 1 to 5 shapes. (**g**) FDTD-simulated EF intensities for S10 under different-wavelength illumination. (**h**) Measured light absorption spectra. Insets: schematic illustration for nanowires of S6 to S10, featuring circular, circular+superelliptic, circular+superelliptic+square, circular+superelliptic+square+star, and circular+superelliptic+square+star+cross shapes. **i**-**l**, Photoelectrocatalytic H_2 production using shape-different TiO_2 nanotubes and Au nanowires (S11 to S15). (**i**) SEM images (left to right): TiO_2 circular nanotubes, TiO_2 square nanotubes, TiO_2 star nanotubes, TiO_2 star nanotubes/Au four-void-circular nanowires, TiO_2 star nanotubes/Au eight-edged-cross nanowires. (**j**) FDTD-simulated EF intensities for TiO_2 nanotubes (linear scale, 350-nm-wavelength illumination) and TiO_2-nanotubes/Au-nanowires (logarithmic scale, 600-nm-wavelength illumination). (**k**) H_2 production rates illuminated by AM 1.5G spectrum and visible light. Error bars show standard deviations. (**l**) Calculated light absorption spectra in TiO_2 nanotubes and TiO_2-nanotubes/Au-nanowires.

Conclusion

Unlike conventional linear spacing-AV relation in aluminium anodization[18], here AV with respect to a specific spacing is altered in a broad range to serve as a controllable 'design knob', which provides a succession of pores with programmable shapes both in-plane and out-of-plane and furthermore enables one to diversify spatial configuration by mixing different pore arrangements and spacings. By systematically programming pore arrangement and shape for each set, a series of pore combinations with different shapes and arrangements can be further obtained. This work not only demonstrates a significant advance of AAO templates which breaks through the dogma 'AAO templates have inherently poor controlling in pore shape, spatial configuration, and combination' but also offers a feasible blueprint that permits the incorporation of uneven

anodization rate designing, broad-range AV adjusting, sequential AV adjusting, mixture arrangement configuring, and wet-chemical after-treatment for future AAO template designing. We believe that the broad selectivity and high controllability of AAO templates and, more importantly, the developed blueprint for template diversification will pave the way towards well-defined nanostructuring over a library of nanostructure arrays, which may be attractive to a wide spectrum of technological applications.

References:

1 Shaltout, A. M., Shalaev, V. M. & Brongersma, M. L. Spatiotemporal light control with active metasurfaces. *Science* **364**, eaat3100 (2019).

2 Cao, Q. *et al.* Arrays of single-walled carbon nanotubes with full surface coverage for high-performance electronics. *Nat. Nanotechnol.* **8**, 180-186 (2013).

3 Shalaev, M. I., Walasik, W., Tsukernik, A., Xu, Y. & Litchinitser, N. M. Robust topologically protected transport in photonic crystals at telecommunication wavelengths. *Nat. Nanotechnol.* **14**, 31-34 (2019).

4 Gu, L. L. *et al.* A biomimetic eye with a hemispherical perovskite nanowire array retina. *Nature* **581**, 278-282 (2020).

5 Mubeen, S. *et al.* An autonomous photosynthetic device in which all charge carriers derive from surface plasmons. *Nat. Nanotechnol.* **8**, 247-251 (2013).

6 Liu, C. *et al.* An all-in-one nanopore battery array. *Nat. Nanotechnol.* **9**, 1031-1039 (2014).

7 Ozin, G. A. & Arsenault, A. *Nanochemistry: a Chemical Approach to Nanomaterials*. (Royal Society of Chemistry, Cambridge, 2015).

8 Liu, N., Tang, M. L., Hentschel, M., Giessen, H. & Alivisatos, A. P. Nanoantenna-enhanced gas sensing in a single tailored nanofocus. *Nat. Mater.* **10**, 631-636 (2011).

9 Ross, M. B., Blaber, M. G. & Schatz, G. C. Using nanoscale and mesoscale anisotropy to engineer the optical response of three-dimensional plasmonic metamaterials. *Nat. Commun.* **5**, 4090 (2014).

10 Bhushan, B. *Springer Handbook of Nanotechnology* (Springer, 2017).

11 Jones, M. R., Osberg, K. D., Macfarlane, R. J., Langille, M. R. & Mirkin, C. A. Templated techniques for the synthesis and assembly of plasmonic nanostructures. *Chem. Rev.* **111**, 3736-3827 (2011).

12 Martin, C. R. Nanomaterials - a membrane-based synthetic approach. *Science* **266**, 1961-1966 (1994).

13 Lee, S. B. *et al.* Antibody-based bio-nanotube membranes for enantiomeric drug separations. *Science* **296**, 2198-2200 (2002).

14 Fan, Z. *et al.* Three-dimensional nanopillar-array photovoltaics on low-cost and flexible substrates. *Nat. Mater.* **8**, 648-653 (2009).

15 Masuda, H. & Fukuda, K. Ordered metal nanohole arrays made by a two-step replication of honeycomb structures of anodic alumina. *Science* **268**, 1466-1468 (1995).

16 Masuda, H. *et al.* Square and triangular nanohole array architectures in anodic alumina. *Adv. Mater.* **13**, 189-192 (2001).

17 Yanagishita, T., Sasaki, M., Nishio, K. & Masuda, H. Carbon nanotubes with a triangular cross-section, fabricated using anodic porous alumina as the template. *Adv. Mater.* **16**, 429-432 (2004).

18 Nielsch, K., Choi, J., Schwirn, K., Wehrspohn, R. B. & Gösele, U. Self-ordering regimes of porous alumina: the 10 porosity rule. *Nano Lett.* **2**, 677-680 (2002).

19 Wen, L., Xu, R., Mi, Y. & Lei, Y. Multiple nanostructures based on anodized aluminium oxide templates. *Nat. Nanotechnol.* **12**, 244-250 (2017).

20 Lee, W. & Park, S.-J. Porous anodic aluminum oxide: anodization and templated synthesis of functional nanostructures. *Chem. Rev.* **114**, 7487-7556 (2014).

21 Vrublevsky, I., Parkoun, V., Sokol, V., Schreckenbach, J. & Marx, G. The study of the volume expansion of aluminum during porous oxide formation at galvanostatic regime. *Appl. Surf. Sci.* **222**, 215-225 (2004).

22 Smith, J. T., Hang, Q., Franklin, A. D., Janes, D. B. & Sands, T. D. Highly ordered diamond and hybrid triangle-diamond patterns in porous anodic alumina thin films. *Appl. Phys. Lett.* **93**, 043108 (2008).

23 Lee, W. *et al.* Structural engineering of nanoporous anodic aluminium oxide by pulse anodization of aluminium. *Nat. Nanotechnol.* **3**, 234-239 (2008).

24 Che, G., Lakshmi, B. B., Fisher, E. R. & Martin, C. R. Carbon nanotubule membranes for electrochemical energy storage and production. *Nature* **393**, 346-349 (1998).

25 Nielsch, K., Muller, F., Li, A. P. & Gosele, U. Uniform nickel deposition into ordered alumina pores by pulsed electrodeposition. *Adv. Mater.* **12**, 582-586 (2000).

26 Daub, M., Knez, M., Goesele, U. & Nielsch, K. Ferromagnetic nanotubes by atomic layer deposition in anodic alumina membranes. *J. Appl. Phys.* **101**, 09J111 (2007).

27 Wang, Z. J. *et al.* Manipulation of charge transfer and transport in plasmonic-ferroelectric hybrids for photoelectrochemical applications. *Nat. Commun.* **7**, 10348 (2016).

28 Nicewarner-Pena, S. R. *et al.* Submicrometer metallic barcodes. *Science* **294**, 137-141 (2001).

29 Qin, L. D., Park, S., Huang, L. & Mirkin, C. A. On-wire lithography. *Science* **309**, 113-115 (2005).

30 Ozel, T., Bourret, G. R. & Mirkin, C. A. Coaxial lithography. *Nat. Nanotechnol.* **10**, 319-324 (2015).

31 Ding, S. Y., You, E. M., Tian, Z. Q. & Moskovits, M. Electromagnetic theories of surface-enhanced Raman spectroscopy. *Chem. Soc. Rev.* **46**, 4042-4076 (2017).

32 Clavero, C. Plasmon-induced hot-electron generation at nanoparticle/metal-oxide interfaces for photovoltaic and photocatalytic devices. *Nat. Photonics* **8**, 95-103 (2014).

Acknowledgments: The authors are grateful to H. Romanus, Dominik Flock, and Diana Herz for helps with FIB cutting, EDX analysis, and argon ion milling. The authors thank J. Döll and A. Konkin for support in optical characterization. The authors thank H. Zhao, H. Zhang, and M. Sommerfeld for technical discussion. This work is financially supported by the German Research Foundation (DFG: LE 2249/5-1) and Sino-German Center for Research Promotion (GZ 1579).

Author contributions: R.X. and Y.L. conceived the concept. Y.L. supervised the project. R.X. conducted the experiments and simulations. Z.Z. helped with device measurement. All authors participated in the discussion on the data. R.X. and Y.L. wrote the manuscript.

Competing interests: The authors declare no competing interests.

Figures

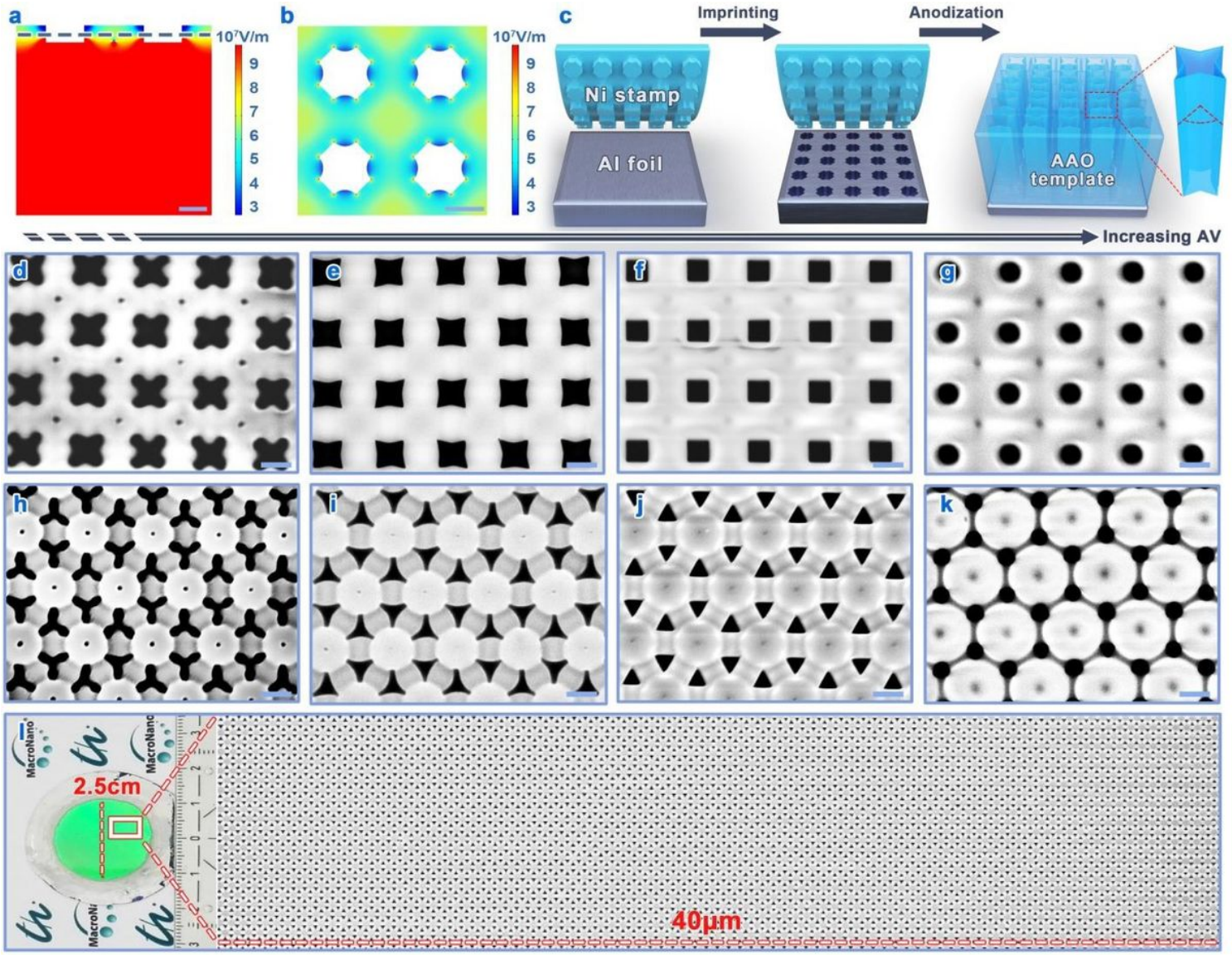

Figure 1

Templates with in-plane shape-programmable pores. a,b, COMSOL-simulated electric fields at (a) vertical cross section and (b) near-surface lateral cross section of an aluminium foil patterned with four-leaf clover-like nanodents of 400-nm spacing and tetragonal arrangement under an anodization voltage (AV) of 120 V, the dashed line in (a) at the half-depth of nanodents marks the near-surface lateral cross section in (b). c, Schematic illustration for the fabrication process of AAO template (from left to right): fabricating Ni imprint stamp and electro-polishing aluminium foil; transferring the structural feature of Ni stamp by imprinting to equip aluminium surface with an array of four-leaf clover-like nanodents; anodizing the imprinted area at different AVs. d-k, SEM images of templates with shape-programmable pores in (d-g) tetragonal and (h-k) hexagonal arrangements. Two arrangements are 400 and 400/√3 nm in spacing, respectively (see Supplementary Figs. 4,7). From left to right, the exploited AVs were incrementally increased, with (d) 120 V, (e) 140 V, (f) 160 V, (g) 200 V; and (h) 100 V, (i) 120 V, (j) 140 V, (k) 155 V,

respectively. l, Optical photograph of 2.5-cm-diameter AAO template (left) and large-area SEM image (right). Scale bars: 200 nm.

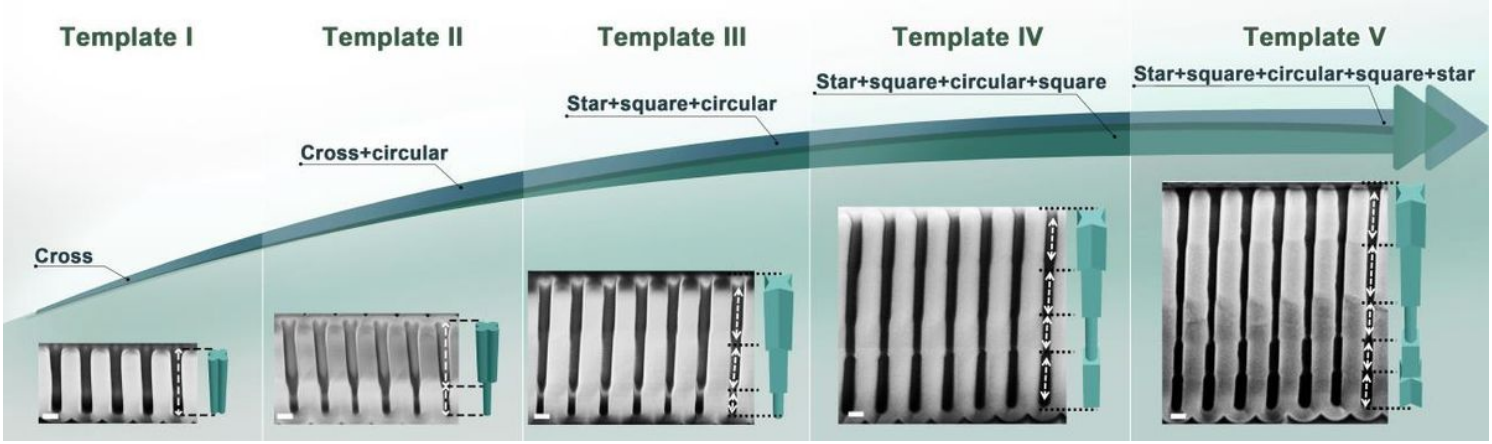

Figure 2

Templates with out-of-plane shape-programmable pores. Cross-sectional SEM images and the corresponding pore schematics (on the right of each SEM figure) of templates I – V with different out-of-plane pore shapes. From left to right: the sequentially exploited AVs (and the pore shapes) are Template I: 120 V (cross); Template II: 120->200 V (cross+circular); Template III: 140->160->200 V (star+square+circular); Template IV: 140->160->200->160 V (star+square+circular+square); Template V: 140->160->200->160->140 V (star+square+circular+square+star), respectively. Scale bars: 200 nm.

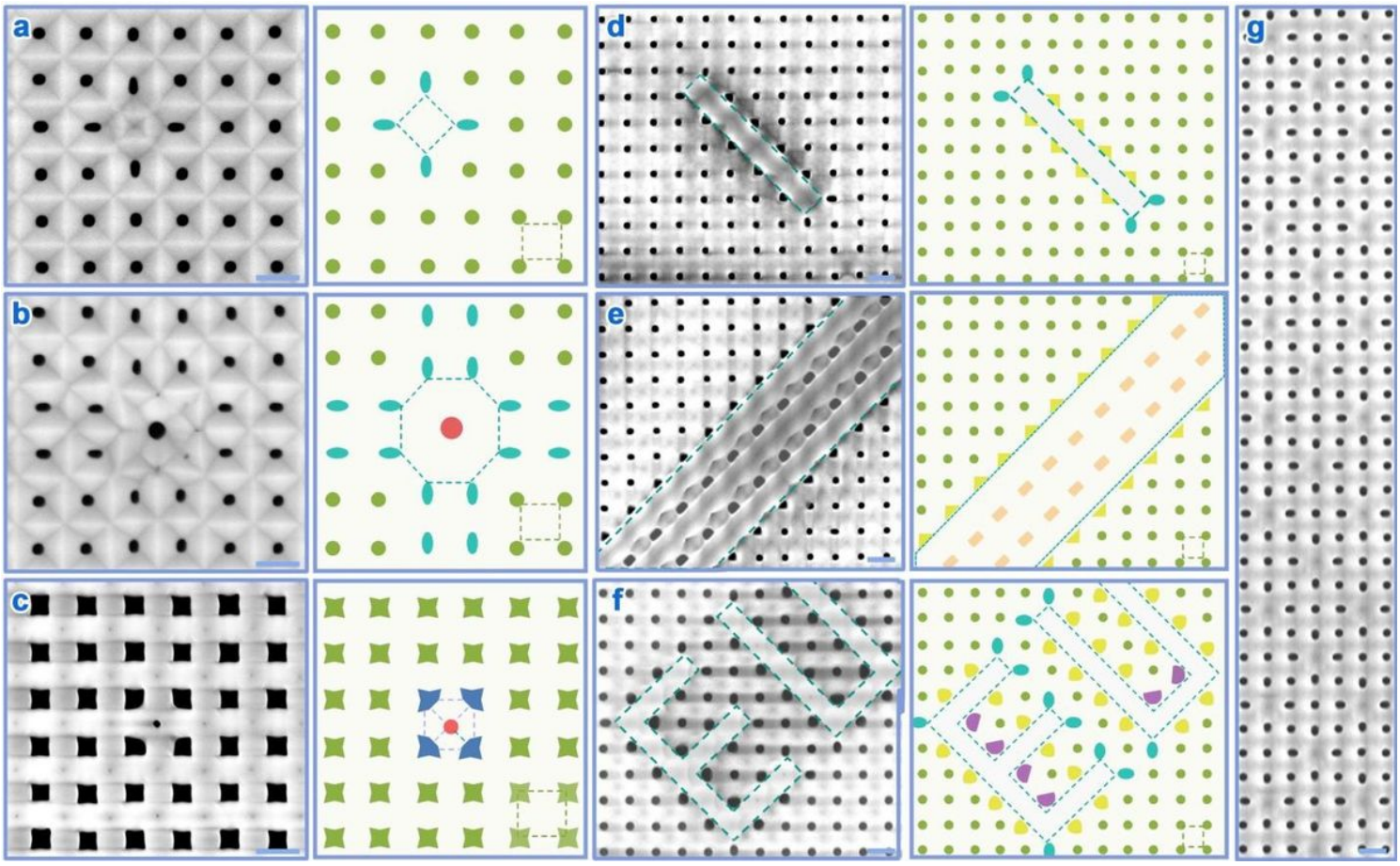

Figure 3

Templates with mixture arrangements. a-f, SEM images (left) and schematics (right) of basic tetragonal templates mixed with accessory point units of (a) larger-spacing tetragonal arrangement, (b) octagonal arrangement, and (c) centered tetragonal arrangement, as well as (d) line, (e) area, and (f) pattern ‘EU’ of larger-spacing tetragonal arrangements. The pores in the basic arrangement are exhibited by green color, and those pores in accessory arrangements are by cyan, red, blue, yellow, orange, and purple colors. g, Large-area SEM image of a mixture of two spacing-different tetragonal arrangements. Scale bars: 400 nm.

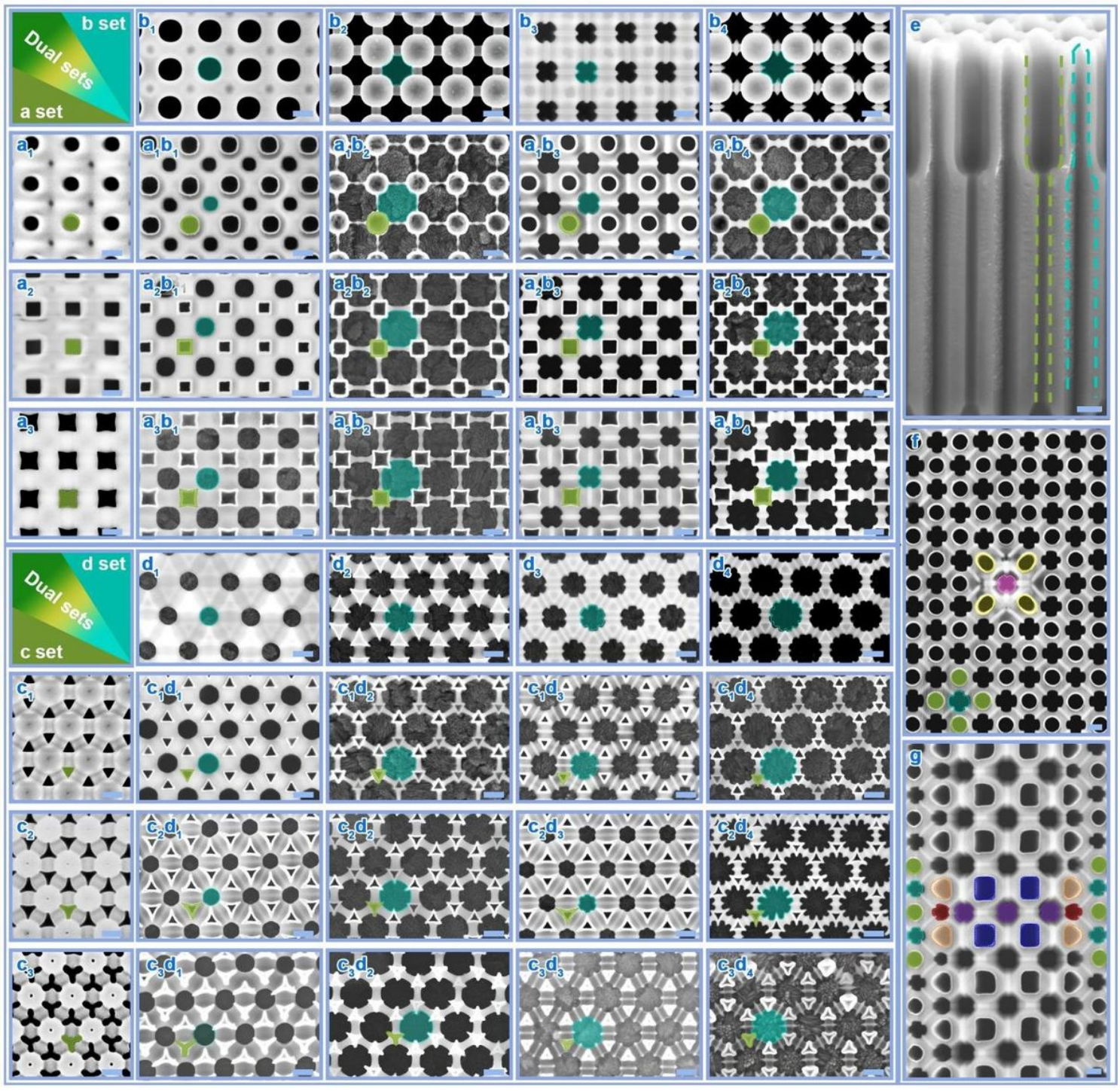

Figure 4

Templates with shape-programmable pore combinations. aibj, Pore combinations, with the 1st-set pores (of tetragonal arrangement, green color) in (ai) (similar to the pores in Fig. 1e-g) and the 2nd-set pores (of tetragonal arrangement, cyan colors) in (bj). The 1st-set and 2nd-set pores were formed before and after the wet-chemical etching procedure, respectively (please refer to Supplementary Fig. 24). cmdn, Pore combinations, with the 1st-set pores (of hexagonal arrangement, green color) in (cm) (similar to the pores in Fig. 1h-j) and the 2nd-set pores (of trigonal arrangements, cyan colors) in (dn). e, Pore combinations with two sets of out-of-plane dual-shape pores outlined by green (1st-set pore) and cyan (2nd-set pore) dashed lines. The anodization for growing the 1st-set pores was performed under sequential AVs of 140->200 V. f,g, Multi-shape pore combinations within mixture arrangements, stemming from the tetragonal templates mixed with point (Fig. 3a) and area (Fig. 3e) units of accessory arrangements. Colors of green/yellow/orange/blue and colors of cyan/pink/purple/red indicate pores formed before and after the wet-chemical etching procedure, respectively. Scale bars: 200 nm.

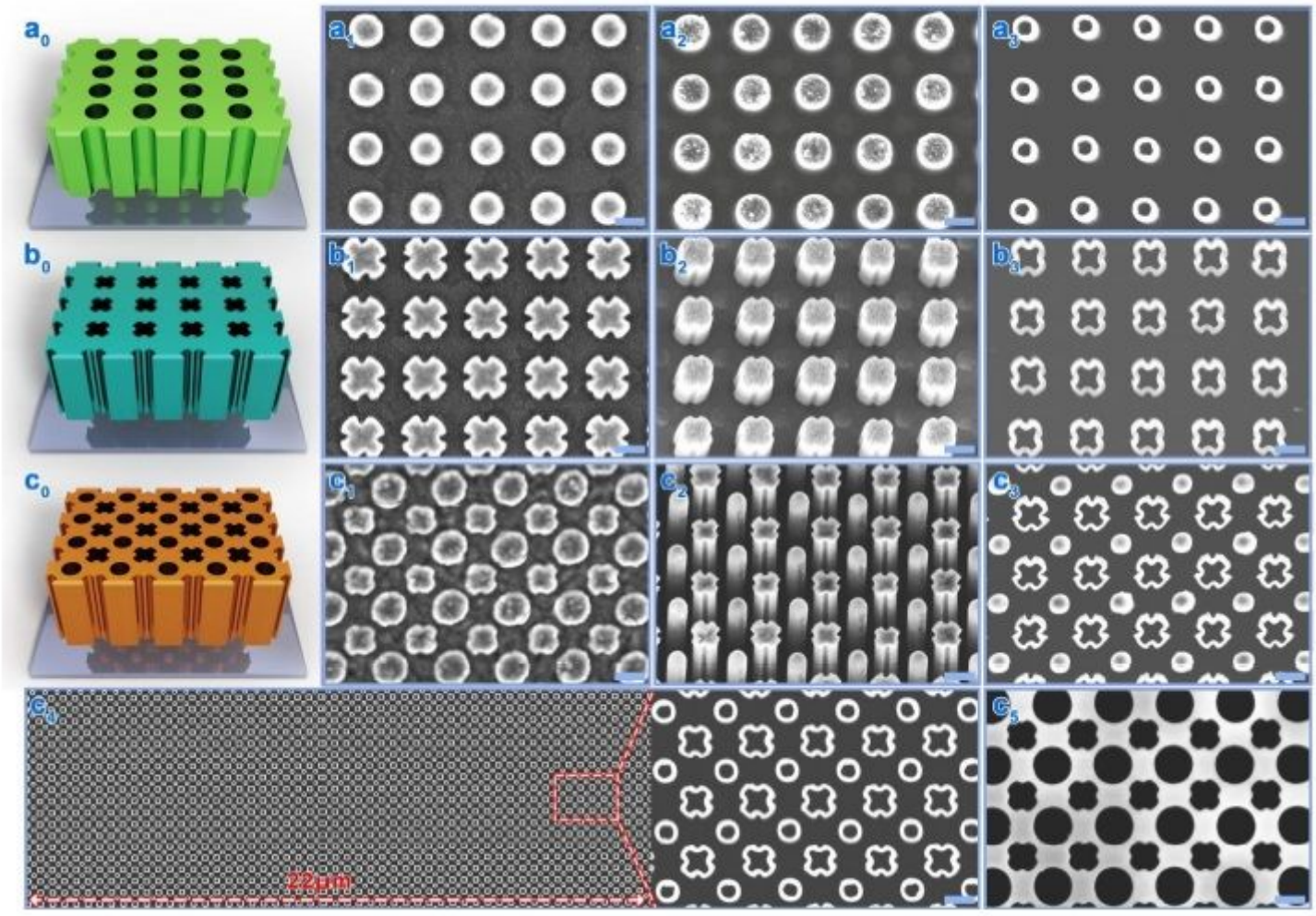

Figure 5

Nanostructure arrays replicated from programmable templates. (a0) Schematic of the template with the 1st-set circular pores and SEM images of the resultant nanostructure arrays: (a1) Au nanoparticles, (a2)

Ni nanowires, and (a3) TiO2 nanotubes. (b0) Schematic of the template with the 2nd-set 4-edged cross-shaped pores and SEM images of the resultant nanostructure arrays: (b1) Au nanoparticles, (b2) Au nanowires, and (b3) SnO2 nanotubes. (c0) Schematic of the template with the two-set pores and SEM images of the resultant nanostructure combinations: (c1) Au-nanoparticles/Au-nanoparticles, (c2) Pt-nanowires/Au-nanowires, (c3) Pt-nanowires/SnO2-nanotubes, (c4) TiO2-nanotubes/SnO2-nanotubes, (c5) Ni dual-pore nanomesh. Scale bars: 200 nm.

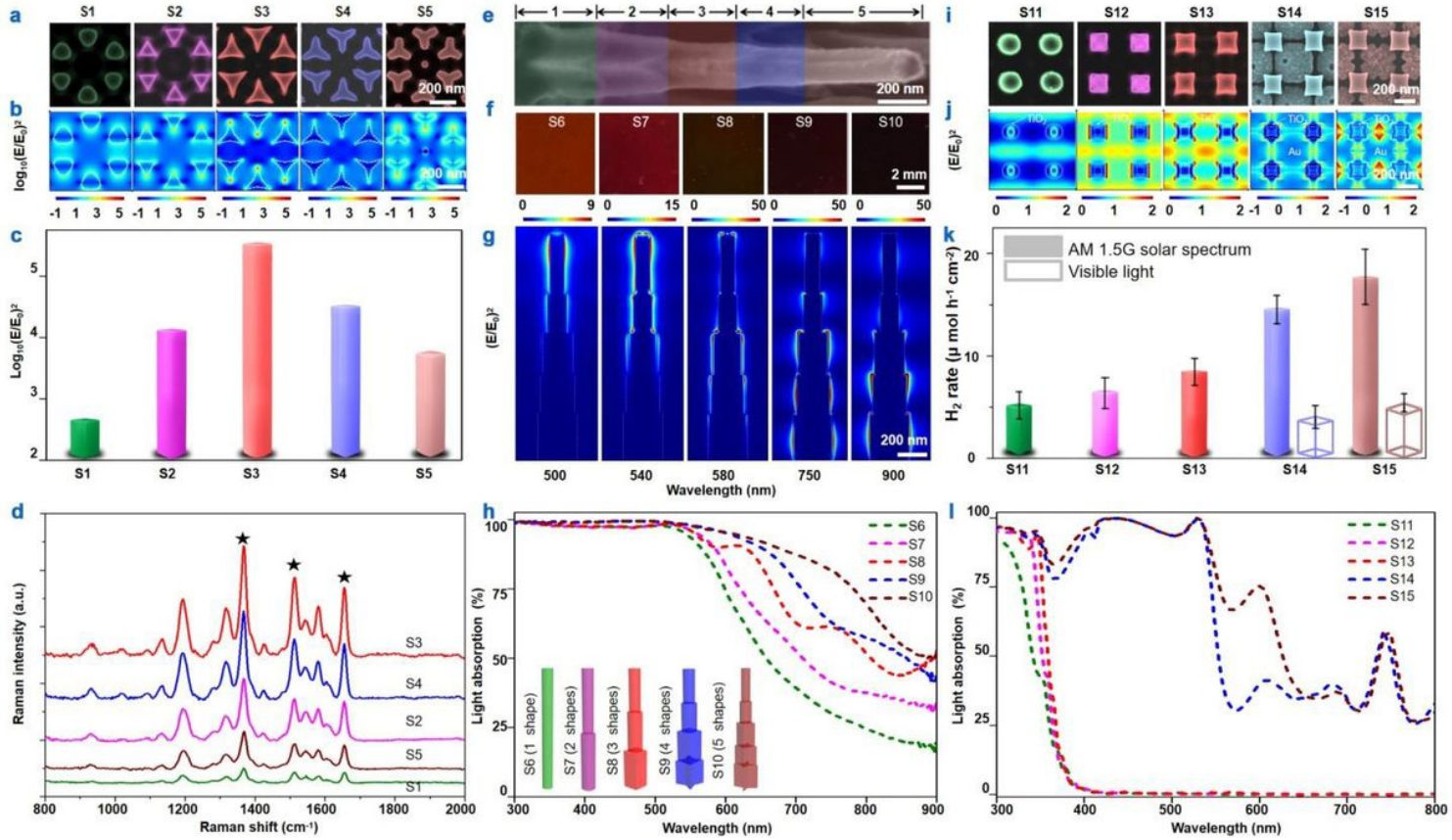

Figure 6

Applications of well-defined nanostructures. a-d, SERS characterization with five hexagonal arrays of in-plane shape-different Ag nanoparticles (S1 to S5). (a) SEM images of unit cells and (b) FDTD-simulated EF intensities (logarithmic scale, 532-nm wavelength illumination). (c) The maximal magnitudes of EF intensities in (b). (d) SERS spectra with three main peaks at 1363, 1508, and 1650 cm−1 for Rhodamine 6G molecules chemisorbed on Ag nanoparticles. e-h, Light absorbers using five tetragonal arrays of out-of-plane shape-different Au nanowires (S6 to S10). (e) SEM image of 5-shape-combined Au nanowire of S10 combining 5 shapes in the axial direction (from left to right): cross, star, square, superelliptic, and circular. (f) Optical photographs of S6 to S10, involving Au nanowires of 1 to 5 shapes. (g) FDTD-simulated EF intensities for S10 under different-wavelength illumination. (h) Measured light absorption spectra. Insets: schematic illustration for nanowires of S6 to S10, featuring circular, circular+superelliptic, circular+superelliptic+square, circular+superelliptic+square+star, and circular+superelliptic+square+star+cross shapes. i-l, Photoelectrocatalytic H2 production using shape-different TiO2 nanotubes and Au nanowires (S11 to S15). (i) SEM images (left to right): TiO2 circular

nanotubes, TiO2 square nanotubes, TiO2 star nanotubes, TiO2 star nanotubes/Au four-void-circular nanowires, TiO2 star nanotubes/Au eight-edged-cross nanowires. (j) FDTD-simulated EF intensities for TiO2 nanotubes (linear scale, 350-nm-wavelength illumination) and TiO2-nanotubes/Au-nanowires (logarithmic scale, 600-nm-wavelength illumination). (k) H2 production rates illuminated by AM 1.5G spectrum and visible light. Error bars show standard deviations. (l) Calculated light absorption spectra in TiO2 nanotubes and TiO2-nanotubes/Au-nanowires.

Supplementary Files

This is a list of supplementary files associated with this preprint. Click to download.

- Supplementaryinformation.pdf